



# Piezoelectrically tuned silicon nitride ring resonator

WARREN JIN,<sup>1,\*</sup> RONALD G. POLCAWICH,<sup>2</sup> PAUL A. MORTON,<sup>3</sup> AND JOHN E. BOWERS<sup>1</sup>

<sup>1</sup>Electrical and Computer Engineering Department, University of California, Santa Barbara, CA 93106, USA

<sup>2</sup>U.S. Army Research Laboratory, Adelphi, MD 20783, USA

<sup>3</sup>Morton Photonics, West Friendship, MD 21794, USA

\*warren@ece.ucsb.edu

**Abstract:** Typical integrated optical phase tuners alter the effective index. In this paper, we explore tuning by geometric deformation. We show that tuning efficiency,  $V_{\pi}L$ , improves as the device size shrinks down to the optimal bend radius, contrary to conventional index-shift based approaches where  $V_{\pi}L$  remains constant. We demonstrate that this approach is capable of ultra-low power tuning across a full FSR in a low-confinement silicon nitride based ring resonator of 580  $\mu\text{m}$  radius. We demonstrate record performance with  $V_{\text{FSR}} = 16 \text{ V}$ ,  $V_{\pi}L = 3.6 \text{ V dB}$ ,  $V_{\pi}L\alpha = 1.1 \text{ V dB}$ , tuning current below 10 nA, and unattenuated tuning response up to 1 MHz. We also present optimized designs for high confinement silicon nitride and silicon based platforms with radius down to 80  $\mu\text{m}$  and 45  $\mu\text{m}$ , respectively, with performance well beyond current state-of-the-art. Applications include narrow-linewidth tunable diode lasers for spectroscopy and non-linear optics, optical phased array beamforming networks for RF antennas and LIDAR, and optical filters for WDM telecommunication links.

© 2018 Optical Society of America under the terms of the [OSA Open Access Publishing Agreement](#)

**OCIS codes:** (130.3120) Integrated optics devices, (230.5750) Resonators, (230.4685) Optical microelectromechanical devices.

## References and links

1. G. Li, X. Zheng, J. Yao, H. Thacker, I. Shubin, Y. Luo, K. Raj, J. E. Cunningham, and A. V. Krishnamoorthy, "25Gb/s 1V-driving CMOS ring modulator with integrated thermal tuning," *Opt. Express* **19**, 20435–20443 (2011).
2. P. Dong, W. Qian, H. Liang, R. Shafiqi, D. Feng, G. Li, J. E. Cunningham, A. V. Krishnamoorthy, and M. Asghari, "Thermally tunable silicon racetrack resonators with ultralow tuning power," *Opt. Express* **18**, 20298–20304 (2010).
3. C. G. Roeloffzen, L. Zhuang, C. Taddei, A. Leinse, R. G. Heideman, P. W. van Dijk, R. M. Oldenbeuving, D. A. Marpaung, M. Burla, and K.-J. Boller, "Silicon nitride microwave photonic circuits," *Opt. Express* **21**, 22937–22961 (2013).
4. N. Hosseini, R. Dekker, M. Hoekman, M. Dekkers, J. Bos, A. Leinse, and R. Heideman, "Stress-optic modulator in TriPleX platform using a piezoelectric lead zirconate titanate (PZT) thin film," *Opt. Express* **23**, 14018–14026 (2015).
5. J. P. Epping, D. Marchenko, A. Leinse, R. Mateman, M. Hoekman, L. Wevers, E. J. Klein, C. G. Roeloffzen, M. Dekkers, and R. G. Heideman, "Ultra-low-power stress-optics modulator for microwave photonics," *Proc. SPIE* **10106**, 101060F (2017).
6. L. Zhuang, C. Roeloffzen, R. Heideman, A. Borreman, A. Meijerink, and W. van Etten, "Single-chip ring resonator-based 1×8 optical beam forming network in CMOS-compatible waveguide technology," *IEEE Photon. Technol. Lett.* **19**, 1130–1132 (2007).
7. P. A. Morton, J. B. Khurgin, Z. Mizrahi, and S. J. Morton, "Commercially packaged optical true-time-delay devices with record delays of wide bandwidth signals," in *CLEO: Applications and Technology* (Optical Society of America, 2014), paper AW3P.6.
8. W. Jin, E. J. Stanton, N. Volet, R. G. Polcawich, P. A. Morton, and J. E. Bowers, "Piezoelectric tuning of a suspended silicon nitride ring resonator," in 2017 IEEE Photonics Conference (IEEE 2017), pp. 117–118.
9. B. A. Auld, *Acoustic Fields and Waves in Solids* (Wiley, 1973).
10. D. A. Berlincourt, D. R. Curran, and H. Jaffe, "Piezoelectric and piezomagnetic materials and their function in transducers," in *Physical Acoustics: Principles and Methods*, vol. 1A, W. P. Mason, ed. (Academic Press, 1964).
11. L. Zhuang, D. Marpaung, M. Burla, W. Beeker, A. Leinse, and C. Roeloffzen, "Low-loss, high-index-contrast  $\text{Si}_3\text{N}_4/\text{SiO}_2$  optical waveguides for optical delay lines in microwave photonics signal processing," *Opt. Express* **19**, 23162–23170 (2011).

12. T. Huffman, D. Baney, and D. J. Blumenthal, "High extinction ratio widely tunable low-loss integrated Si<sub>3</sub>N<sub>4</sub> third-order filter," arXiv preprint arXiv:1708.06344 (2017).
13. S. Trolier-McKinstry and P. Muralt, "Thin film piezoelectrics for MEMS," J. Electroceram. **12**, 7–17 (2004).
14. R. Dixon, "Photoelastic properties of selected materials and their relevance for applications to acoustic light modulators and scanners," J. Appl. Phys. **38**, 5149–5153 (1967).
15. W. Cook, D. Nelson, and K. Vedam, *Piezooptic and Electrooptic Constants*, vol. 30 (Springer, 1996).
16. B. Melnick, C. P. de Araujo, L. McMillan, D. Carver, and J. Scott, "Recent results on switching, fatigue and electrical characterization of sol-gel based PZT capacitors," Ferroelectrics **116**, 79–93 (1991).
17. H. D. Chen, K. Udayakumar, K. K. Li, C. J. Gaskey, and L. E. Cross, "Dielectric breakdown strength in sol-gel derived PZT thick films," Integr. Ferroelectr. **15**, 89–98 (1997).
18. R. Moazzami, C. Hu, and W. H. Shepherd, "Electrical characteristics of ferroelectric PZT thin films for DRAM applications," IEEE Trans. Electron Devices **39**, 2044–2049 (1992).
19. T. Chen, H. Lee, and K. J. Vahala, "Thermal stress in silica-on-silicon disk resonators," Appl. Phys. Lett. **102**, 031113 (2013).
20. S. S. Azadeh, F. Merget, S. Romero-García, A. Moscoso-Mártir, N. von den Driesch, J. Müller, S. Mantl, D. Buca, and J. Witzens, "Low V<sub>π</sub> silicon photonics modulators with highly linear epitaxially grown phase shifters," Opt. Express **23**, 23526–23550 (2015).
21. G. T. Reed, G. Z. Mashanovich, F. Y. Gardes, M. Nedeljkovic, Y. Hu, D. J. Thomson, K. Li, P. R. Wilson, S.-W. Chen, and S. S. Hsu, "Recent breakthroughs in carrier depletion based silicon optical modulators," Nanophotonics **3**, 229–245 (2014).
22. M. A. Webster, K. Lakshmikummar, C. Appel, C. Muzio, B. Dama, and K. Shastri, "Low-power MOS-capacitor based silicon photonic modulators and CMOS drivers," in Optical Fiber Communication Conference (Optical Society of America, 2015), paper W4H.3.
23. L. Zhang, J. Sinsky, D. Van Thourhout, N. Sauer, L. Stulz, A. Adamiecki, and S. Chandrasekhar, "Low-voltage high-speed travelling wave InGaAsP-InP phase modulator," IEEE Photon. Technol. Lett. **16**, 1831–1833 (2004).
24. T. Hiraki, T. Aihara, K. Hasebe, K. Takeda, T. Fujii, T. Kakitsuka, T. Tsuchizawa, H. Fukuda, and S. Matsuo, "Heterogeneously integrated III–V/Si MOS capacitor Mach–Zehnder modulator," Nat. Photon. **11**, 482–485 (2017).
25. J. Liu, G. Xu, F. Liu, I. Kityk, X. Liu, and Z. Zhen, "Recent advances in polymer electro-optic modulators," RSC Adv. **5**, 15784–15794 (2015).
26. R. Ding, T. Baehr-Jones, W.-J. Kim, A. Spott, M. Fournier, J.-M. Fedeli, S. Huang, J. Luo, A. K.-Y. Jen, L. Dalton, and M. Hochberg, "Sub-volt silicon-organic electro-optic modulator with 500 MHz bandwidth," J. Lightw. Technol. **29**, 1112–1117 (2011).
27. R. Palmer, S. Koeber, D. L. Elder, M. Woessner, W. Heni, D. Korn, M. Lauermann, W. Bogaerts, L. Dalton, W. Freude, J. Leuthold, and C. Koos, "High-speed, low drive-voltage silicon-organic hybrid modulator based on a binary-chromophore electro-optic material," J. Lightw. Technol. **32**, 2726–2734 (2014).
28. A. Rao, A. Patil, J. Chiles, M. Malinowski, S. Novak, K. Richardson, P. Rabiei, and S. Fathpour, "Heterogeneous microring and Mach-Zehnder modulators based on lithium niobate and chalcogenide glasses on silicon," Opt. Express **23**, 22746–22752 (2015).
29. P. Tang, D. Towner, T. Hamano, A. Meier, and B. Wessels, "Electrooptic modulation up to 40 GHz in a barium titanate thin film waveguide modulator," Opt. Express **12**, 5962–5967 (2004).
30. C. Xiong, W. H. Pernice, J. H. Ngai, J. W. Reiner, D. Kumah, F. J. Walker, C. H. Ahn, and H. X. Tang, "Active silicon integrated nanophotonics: ferroelectric BaTiO<sub>3</sub> devices," Nano Lett. **14**, 1419–1425 (2014).
31. G. Jin, Y. Zou, V. Ffullyigin, S. Liu, Y. Lu, J. Zhao, and M. Cronin-Golomb, "PLZT film waveguide Mach-Zehnder electrooptic modulator," J. Lightw. Technol. **18**, 807 (2000).
32. K. Alexander, J. P. George, B. Kuyken, J. Beeckman, and D. Van Thourhout, "Broadband electro-optic modulation using low-loss PZT-on-silicon nitride integrated waveguides," in CLEO: Applications and Technology (Optical Society of America, 2017), paper JTh5C.7.
33. R. S. Jacobsen, K. N. Andersen, P. I. Borel, J. Fage-Pedersen, L. H. Frandsen, O. Hansen, M. Kristensen, A. V. Lavrinenko, G. Moulin, H. Ou, C. Peucheret, B. Zsgiri, and A. Bjarklev, "Strained silicon as a new electro-optic material," Nature **441**, 199–202 (2006).
34. B. Chmielak, C. Matheisen, C. Ripperda, J. Bolten, T. Wahlbrink, M. Waldow, and H. Kurz, "Investigation of local strain distribution and linear electro-optic effect in strained silicon waveguides," Opt. Express **21**, 25324–25332 (2013).
35. C. Xiong, W. H. Pernice, X. Sun, C. Schuck, K. Y. Fong, and H. X. Tang, "Aluminum nitride as a new material for chip-scale optomechanics and nonlinear optics," New J. Phys. **14**, 095014 (2012).
36. S. Zhu and G.-Q. Lo, "Aluminum nitride electro-optic phase shifter for backend integration on silicon," Opt. Express **24**, 12501–12506 (2016).
37. G. N. Nielson, D. Seneviratne, F. Lopez-Royo, P. T. Rakich, Y. Avrahami, M. R. Watts, H. A. Haus, H. L. Tuller, and G. Barbastathis, "Integrated wavelength-selective optical MEMS switching using ring resonator filters," IEEE Photon. Technol. Lett. **17**, 1190–1192 (2005).
38. S. C. Abdulla, L. Kauppinen, M. Dijkstra, M. J. de Boer, E. Berenschot, H. V. Jansen, R. De Ridder, and G. J. Krijnen, "Tuning a racetrack ring resonator by an integrated dielectric MEMS cantilever," Opt. Express **19**, 15864–15878 (2011).

39. C. Errando-Herranz, F. Niklaus, G. Stemme, and K. B. Gylfason, "A low-power MEMS tunable photonic ring resonator for reconfigurable optical networks," in Proceedings of the 28th IEEE International Conference on Micro Electro Mechanical Systems (IEEE, 2015), pp. 53–56.
40. H. Du, F. S. Chau, and G. Zhou, "Mechanically-tunable photonic devices with on-chip integrated MEMS/NEMS actuators," *Micromachines* **7**, 69 (2016).
41. S. Han, T. J. Seok, N. Quack, B.-W. Yoo, and M. C. Wu, "Large-scale silicon photonic switches with movable directional couplers," *Optica* **2**, 370–375 (2015).
42. T. Ikeda and K. Hane, "A microelectromechanically tunable microring resonator composed of freestanding silicon photonic waveguide couplers," *Appl. Phys. Lett.* **102**, 221113 (2013).
43. M. C. Huang, Y. Zhou, and C. J. Chang-Hasnain, "A nanoelectromechanical tunable laser," *Nat. Photon.* **2**, 180–184 (2008).
44. V. Jayaraman, G. Cole, M. Robertson, C. Burgner, D. John, A. Uddin, and A. Cable, "Rapidly swept, ultra-widely-tunable 1060 nm MEMS-VCSELs," *Electron. Lett.* **48**, 1331–1333 (2012).
45. X. Zheng, V. Kaman, S. Yuan, Y. Xu, O. Jerphagnon, A. Keating, R. C. Anderson, H. N. Poulsen, B. Liu, J. R. Sechrist, C. Pulara, R. Helkey, D. J. Blumenthal, and J. E. Bowers, "Three-dimensional MEMS photonic cross-connect switch design and performance," *IEEE J. Sel. Topics Quantum Electron.* **9**, 571–578 (2003).
46. M. Datta, M. Pruessner, K. Amarnath, J. McGee, S. Kanakaraju, and R. Ghodssi, "Wavelength-selective integrated optical MEMS filter in InP," in Proceedings of the 18th IEEE International Conference on Micro Electro Mechanical Systems (IEEE 2005), pp. 88–91.
47. K. Tsia, S. Fathpour, and B. Jalali, "Electrical tuning of birefringence in silicon waveguides," *Appl. Phys. Lett.* **92**, 061109 (2008).
48. Y. Sebbag, I. Goykhman, B. Desiatov, T. Nachmias, O. Yoshaei, M. Kabla, S. Meltzer, and U. Levy, "Bistability in silicon microring resonator based on strain induced by a piezoelectric lead zirconate titanate thin film," *Appl. Phys. Lett.* **100**, 141107 (2012).
49. S. Donati, L. Barbieri, and G. Martini, "Piezoelectric actuation of silica-on-silicon waveguide devices," *IEEE Photon. Technol. Lett.* **10**, 1428–1430 (1998).
50. B. Dong, H. Tian, M. Zervas, T. J. Kippenberg, and S. A. Bhave, "PORT: a piezoelectric optical resonance tuner," presented at the 31st IEEE International Conference on Micro Electro Mechanical Systems, Belfast, Northern Ireland, 21–25 Jan. 2018.
51. H. Lee, T. Chen, J. Li, K. Y. Yang, S. Jeon, O. Painter, and K. J. Vahala, "Chemically etched ultrahigh-Q wedge-resonator on a silicon chip," *Nat. Photon.* **6**, 369–373 (2012).
52. K. Y. Yang, D. Y. Oh, S. H. Lee, Q.-F. Yang, X. Yi, and K. Vahala, "Integrated ultra-high-Q optical resonator," arXiv preprint arXiv:1702.05076 (2017).
53. J.-F. Veyan, M. Halls, S. Rangan, D. Aureau, X.-M. Yan, and Y. Chabal, "XeF<sub>2</sub>-induced removal of SiO<sub>2</sub> near Si surfaces at 300 K: An unexpected proximity effect," *J. Appl. Phys.* **108**, 114914 (2010).
54. P. Dong, W. Qian, S. Liao, H. Liang, C.-C. Kung, N.-N. Feng, R. Shafiqi, J. Fong, D. Feng, A. V. Krishnamoorthy, and M. Asghari, "Low loss shallow-ridge silicon waveguides," *Opt. Express* **18**, 14474–14479 (2010).
55. G. Li, J. Yao, H. Thacker, A. Mekis, X. Zheng, I. Shubin, Y. Luo, J.-H. Lee, K. Raj, J. E. Cunningham, and A. V. Krishnamoorthy, "Ultralow-loss, high-density SOI optical waveguide routing for macrochip interconnects," *Opt. Express* **20**, 12035–12039 (2012).
56. S. K. Selvaraja, G. Winroth, S. Locorotondo, G. Murdoch, A. Milenin, C. Delvaux, P. Ong, S. Pathak, W. Xie, G. Sterckx, G. Lepage, D. V. Thourhout, W. Bogaerts, J. V. Campenhout, and P. Absil, "193nm immersion lithography for high performance silicon photonic circuits," in Proc. SPIE **9052**, 90520F.1 (2014).
57. X. Ji, F. A. Barbosa, S. P. Roberts, A. Dutt, J. Cardenas, Y. Okawachi, A. Bryant, A. L. Gaeta, and M. Lipson, "Ultra-low-loss on-chip resonators with sub-milliwatt parametric oscillation threshold," *Optica* **4**, 619–624 (2017).
58. L. M. Sanchez, D. M. Potrepka, G. R. Fox, I. Takeuchi, K. Wang, L. A. Bendersky, and R. G. Polcawich, "Optimization of PbTiO<sub>3</sub> seed layers and Pt metallization for PZT-based piezoMEMS actuators," *J. Mater. Res.* **28**, 1920–1931 (2013).
59. G. R. Fox, D. M. Potrepka, and R. G. Polcawich, "Dependence of {111}-textured Pt electrode properties on TiO<sub>2</sub> seed layers formed by thermal oxidation," *J. Mater. Sci. Mater. Electron.* pp. 1–15 (2017).
60. K. Budd, S. Dey, and D. Payne, "Sol-gel processing of PbTiO<sub>3</sub>, PbZrO<sub>3</sub>, PZT, and PLZT thin films," in British Ceramic Proceedings, B. Steele, ed. (Inst of Ceramics, 1985), pp. 107–121.
61. S. K. Dey, K. D. Budd, and D. A. Payne, "Thin-film ferroelectrics of PZT of sol-gel processing," *IEEE Trans. Ultrason., Ferroelect., Freq. Control* **35**, 80–81 (1988).

## 1. Introduction

Ultra-low loss integrated photonic platforms are universally hamstrung by a lack of effective phase tuning mechanisms. The typical thermo-optic tuning approach requires 1 to 100 mW per free spectral range (FSR) per device in silicon-based platforms [1, 2], and 200 to 500 mW per FSR per device in silicon nitride-based platforms [3]. Electro-optic or charge-carrier-based

approaches tend to increase propagation loss and degrade device performance. Demonstrations of tuning by the photoelastic effect show low propagation losses and low tuning power, however the effect is weak, requiring impractically long devices to tune by a full FSR [4, 5]. Real-world optical beamforming networks for RF antennas [6, 7] would require thousands of devices [3], so low tuning power, low optical loss, and small size are required for practical applications. In this work, we will show that all three requirements may be simultaneously satisfied by a purely geometric tuning approach. We demonstrate this by incorporating a PZT thin film piezoelectric actuator with suspended waveguides. In [8], we presented preliminary static tuning results. In what follows, we will present the theory, detailed analysis of the design, and comparison with current state of the art.

## 2. Theory

Within an optical resonator, the resonance condition is expressed as

$$Ln_{\text{eff}} = m\lambda \quad (1)$$

where  $L$  is the round-trip device length,  $n_{\text{eff}}$  the effective index of the optical mode,  $\lambda$  the free-space wavelength,  $m$  the longitudinal mode number and a positive integer. This results in a periodic array of resonance wavelengths, with spacing given by the free spectral range (FSR)

$$\Delta\lambda_{\text{FSR}} = \frac{\lambda^2}{n_{\text{g,eff}}L} \quad (2)$$

where  $n_{\text{g,eff}}$  is the effective group index. Tunability by an FSR, representing a  $2\pi$  phase shift, is a critical metric, as it allows for aligning a resonance to any arbitrary wavelength. Equivalently, tuning by an FSR corresponds to changing the longitudinal mode number by exactly 1 for fixed wavelength, that is,

$$\Delta m = 1 \quad (3)$$

$$\Delta\lambda = 0 \quad (4)$$

Differentiating Eq. (1), and substituting Eq. (3) and Eq. (4), we obtain

$$L\Delta n_{\text{eff}} + n_{\text{eff}}\Delta L = \lambda \quad (5)$$

Typical approaches to tuning employ the first term on the left hand side of Eq. (5). Instead, we target the second term on the left hand side of Eq. (5). By fabricating a piezoelectric actuator on a suspended membrane containing an optical ring resonator, we form a radially symmetric unimorph cantilever structure, shown in Fig. 1. In a piezoelectric material, electric fields are related to mechanical deformation through [9, 10].

$$T = -\underline{e}E + c^E S \quad (6)$$

$$D = eS + \epsilon^S E \quad (7)$$

where  $e$  and  $\underline{e}$  are piezoelectric stress tensors,  $S$  the strain tensor,  $T$  the stress tensor,  $c^E$  the stiffness tensor,  $D$  the electrical displacement vector,  $E$  the electric field vector, and  $\epsilon^S$  the dielectric permittivity tensor. With the application of an electric field across the actuator, an in-plane contraction of the piezoelectric causes the structure to curl upwards (Fig. 1(c), 1(d)). This upwards displacement is accompanied by a radial displacement,  $\Delta R$ , (Fig. 1(e)), and corresponding contraction in the path length of the ring resonator,  $\Delta L$ , given by

$$\Delta L = 2\pi\Delta R \quad (8)$$

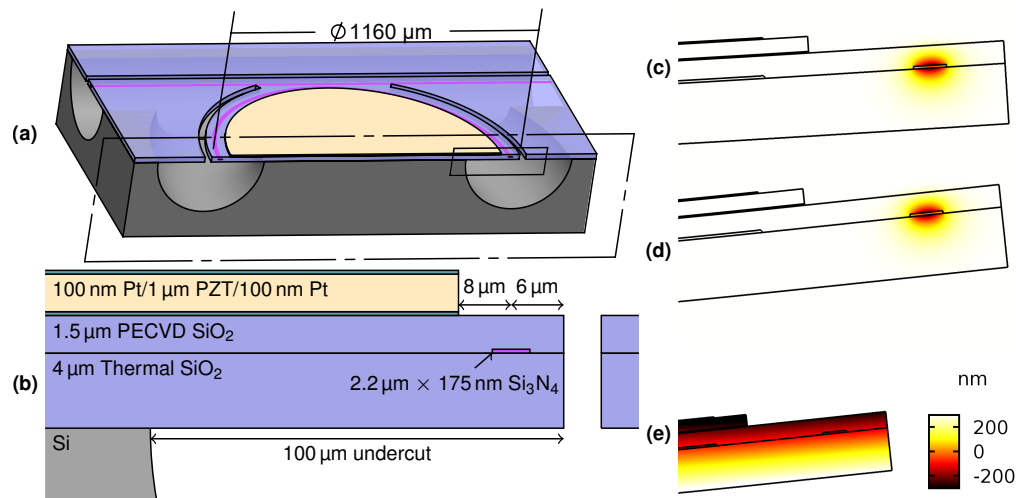


Fig. 1. Geometry for fabricated devices. Undercut of the ring allows the resonator to deform, straining the waveguide and tuning the optical resonance. (a) The geometry is roughly symmetric about the dashed cross-section plane. Devices were designed with two coupled bus waveguides in the add-drop configuration. (b) Detail view of the area denoted by solid rectangle in (a). Simulated TM optical mode profile and device shape under 0V (c) and 16V (d) applied bias to PZT actuator. (e) radial displacement in nm between (c) and (d).

Ignoring any perturbation to the effective index ( $\Delta n_{\text{eff}} = 0$ ), and substituting Eq. (8) into Eq. (5) we observe that the required radial displacement for tuning by an FSR is in fact independent of device size and is given by

$$\Delta R = \frac{\lambda}{2\pi n_{\text{eff}}} \quad (9)$$

To explore the relationship between tuning efficiency and device size, we consider a fixed cross sectional geometry (as in Fig. 1(b)), fixed tuning voltage, and fixed released membrane distance, changing only the bend radius. We note that even a device approaching infinite bend radius (corresponding to a straight waveguide) still experiences a radial (i.e. lateral) displacement under applied voltage that is identical to the lateral displacement of a unimorph cantilever beam with the same cross-section. Thus, in the limit of large bend radii, we expect the radial displacement to be independent of device radius.

Since the required radial displacement for tuning by an FSR in Eq. (9), and the radial displacement itself are both independent of device radius, we conclude that a device design tunable by an FSR remains tunable by an FSR as device size is reduced, so long as the bend radius is large. However, since FSR grows as the device size is reduced in Eq. (2), this leads to the counterintuitive result that the tuning range of the device actually improves as the device size is reduced. When the device radius becomes comparable to the released distance, the structure will stiffen as the radius is further reduced and eventually the ratio of tuning range to FSR will fall. We show in the following section that there is an optimal bend radius, on the order of the release distance, for which the absolute tuning range is maximized.

In contrast, tuning caused by electro-optic effect is linearly proportional to applied voltage and interaction length, leading to a natural figure of merit  $V_{\pi}L$  which remains constant as device length is changed, where  $V_{\pi}$  is the voltage required to induce a  $\pi$  phase shift. Borrowing this same figure of merit, we find that in the large radius limit of this proposed structure,  $V_{\pi}L$  in fact

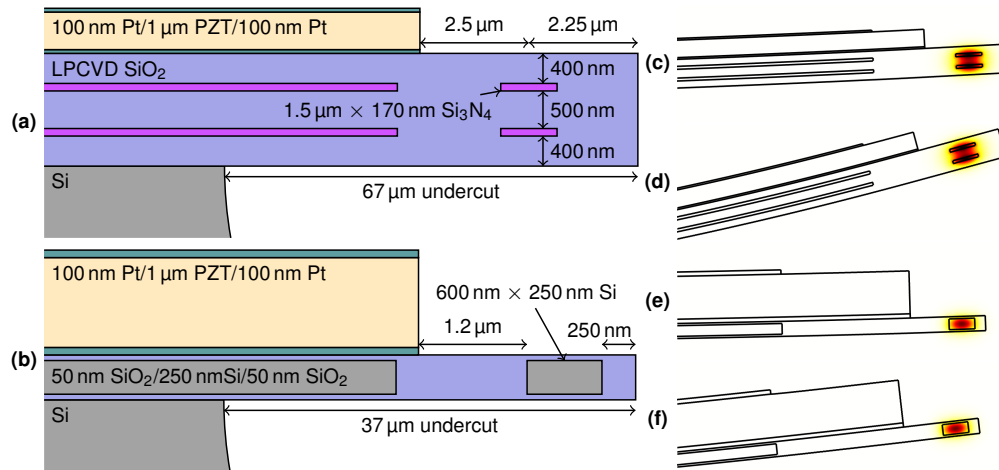


Fig. 2. Geometry for proposed devices. (a) cross-sectional geometry based on dual strip SiN waveguide of [11]. (b) cross-sectional geometry based on deeply etched SOI waveguides. TE mode within the dual-strip nitride waveguide under 0V (c) and 30V (d) bias. TE mode within the silicon waveguide under 0V (e) and 30V (f) bias.

decreases proportionally as we reduce the device length, and it is  $V_\pi$  that remains constant.

### 3. Design

To demonstrate this principle, we select the high-aspect-ratio  $\text{Si}_3\text{N}_4$  waveguide platform of [12]. However, since we hope to induce a significant geometric deformation of the structure, we choose thinner upper and lower claddings of  $1.5\ \mu\text{m}$  and  $4\ \mu\text{m}$ , respectively. For the piezoelectric we select PZT due to its large piezoelectric coefficient  $e_{31,f}$  of  $-8$  to  $-12\ \text{C}/\text{m}^2$ , an order of magnitude better than other readily available strongly piezoelectric materials such as AlN ( $e_{31,f} = -1.05\ \text{C}/\text{m}^2$ ) or ZnO ( $e_{31,f} = -1.00\ \text{C}/\text{m}^2$ ) [13]. The designed geometry and mode profile of the fabricated structure is shown in Fig. 1(a), 1(b), 1(c). To explore the limits of the approach, we will also consider the dual-stripe  $\text{Si}_3\text{N}_4$  platform of [11], and a deeply etched silicon-on-insulator (SOI) waveguide platform, shown in Fig. 2(a) and 2(b), respectively. For each design we choose a fixed undercut distance and maximum applied voltage, and simulate the tuning range as a function of bend radius. Finite-element-method simulations were carried out at  $1550\ \text{nm}$  in cylindrically symmetric geometry, incorporating simultaneous effects of mechanical deformation as well as photoelastic index shift. The photoelastic coefficients of amorphous  $\text{Si}_3\text{N}_4$  are unknown in the literature; as a coarse approximation, they were assumed equal to the photoelastic coefficients of  $\text{SiO}_2$ . The photoelastic coefficients of  $\text{SiO}_2$  used were  $p_{11} = 0.121$ ,  $p_{12} = 0.270$ ,  $p_{44} = -0.075$  [14], whereas the photoelastic coefficients of Si used were  $p_{11} = -0.094$ ,  $p_{12} = 0.017$ ,  $p_{44} = -0.051$  [15]. Otherwise, standard literature values for the mechanical and optical properties of Si,  $\text{SiO}_2$ ,  $\text{Si}_3\text{N}_4$ , Pt, and PZT-5H were used. For the design of Fig. 1,  $16\ \text{V}$  was chosen as the simulation voltage, as it was the voltage for which we demonstrated tuning by a full FSR. For the other designs, a simulation voltage of  $30\ \text{V}$  was chosen, for a field of  $300\ \text{kV}/\text{cm}$  consistent with the dielectric strength of high quality PZT films [16–18].

In Fig. 3(a), 3(c), 3(e), we observe that the ratio of wavelength tuning to FSR is independent of bend radius when the radius is much larger than the undercut distance, consistent with our prediction of constant  $V_\pi$  for large radii. However, even as the radius approaches the undercut distance, the wavelength tuning range continues to improve, as shown in Fig. 3(b), 3(d), 3(f). Tuning efficiency improves as the device shrinks. To quantify the impact of the photoelastic effect,

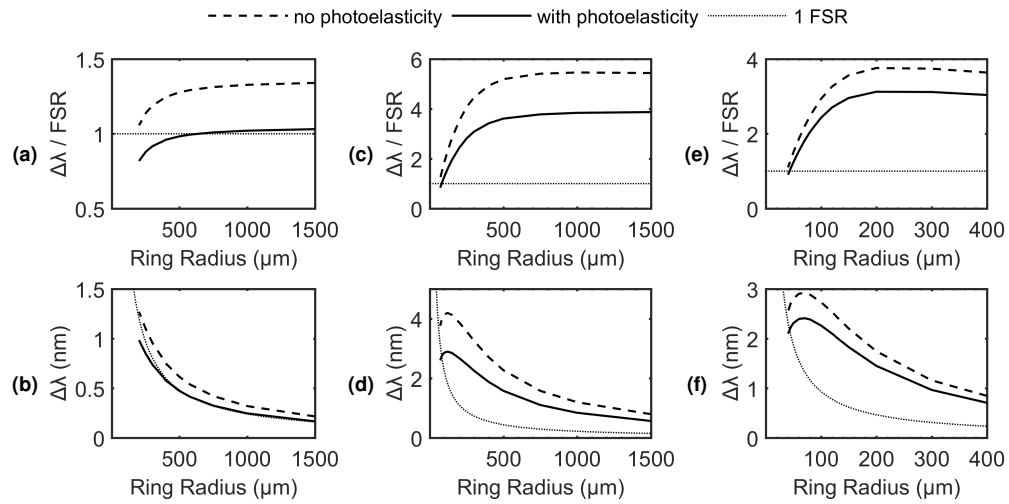


Fig. 3. Simulated tuning range versus ring radius for fixed undercut distance and voltage for each design. Tuning range as (a) a fraction of FSR and (b) in nm for the fabricated single-stripe nitride waveguide design (100  $\mu\text{m}$  undercut, 16 V bias). Tuning range as (c) a fraction of FSR and (d) in nm for the proposed dual-stripe design (67  $\mu\text{m}$  undercut, 30 V bias). Tuning range as (e) a fraction of FSR and (f) in nm for the proposed Si waveguide design (37  $\mu\text{m}$  undercut, 30 V bias). In each case, the tuning penalty due to photoelastic effect is between 15 to 30% of the total tuning range. When expressed as a fraction of FSR in (a), (c), and (e), the tuning range is independent of ring radius for large radii. When expressed in absolute terms in (b), (d), and (f), the tuning range tends to improve as ring radius shrinks.

Table 1. Parameters and results for the simulations shown in Fig. 3. For each design, we determine the minimum bend radius tunable by a full FSR. At this minimum bend radius, we also simulate the fundamental mechanical resonance frequency to determine the maximum tuning speed.

Platform	Simulation parameters	Minimum bend radius	Fundamental mechanical resonance
Single-stripe $\text{Si}_3\text{N}_4$	100 $\mu\text{m}$ undercut 16 V bias	580 $\mu\text{m}$	550 kHz at 0 V 550 kHz at 16 V
Dual-stripe $\text{Si}_3\text{N}_4$	67 $\mu\text{m}$ undercut 30 V bias	80 $\mu\text{m}$	500 kHz at 0 V 720 kHz at 30 V
SOI	37 $\mu\text{m}$ undercut 30 V bias	45 $\mu\text{m}$	780 kHz at 0 V 1100 kHz at 30 V

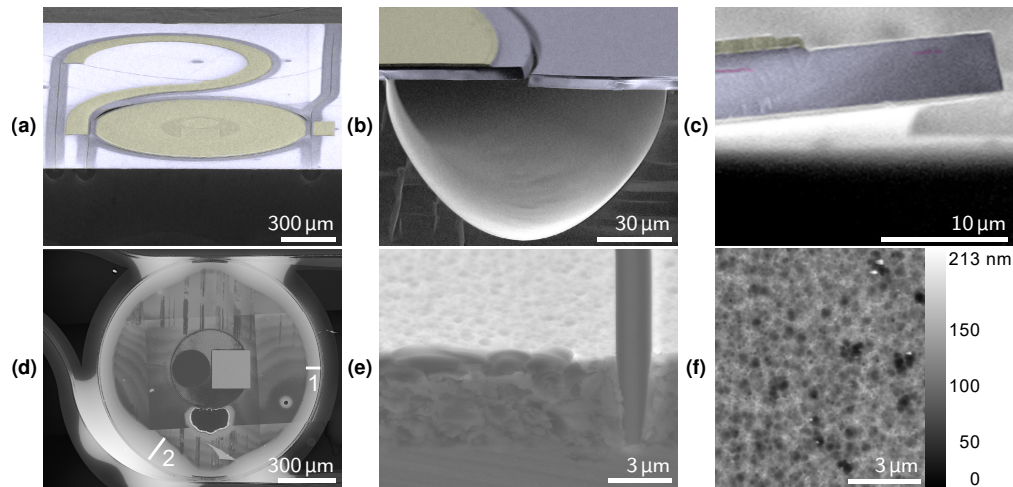


Fig. 4. Fabricated device images. SEM (colorized) images have been tinted: actuator-yellow,  $\text{SiO}_2$ -blue,  $\text{Si}_3\text{N}_4$ -magenta. (a) SEM image – oblique view. (b) Cleaved ring resonator. (c) Cleaved waveguide core. (d) Height map by confocal microscopy with image stitching. The color scale is non-linear, to emphasize vertical displacement at the actuator surface. The distances marked 1 and 2,  $75\ \mu\text{m}$  and  $155\ \mu\text{m}$  respectively, indicate the approximate undercut in those regions. (e) SEM image of cladding, left rough by PZT actuator processing, adjacent to an etched trench and diced facet. (f) AFM heightmap of rough upper surface. The rough surface impacts propagation loss, but process optimizations should remedy it.

the same simulations have been performed setting photoelastic constants  $p_{11} = p_{12} = p_{44} = 0$ , and the results displayed by the dashed traces in Fig. 3. In all cases, the photoelastic effect represents a tuning penalty ranging from 15 to 30% of the total tuning range, represented by the difference between solid and dashed traces in Fig. 3. For each design, a minimum bend radius tunable by a full FSR was determined, shown in Table 1. For released membranes under net compressive stress, buckling of the membrane may occur [19]. For the minimum bend radius of each design, a full 3D solid mechanics simulation was performed to confirm that the membranes do not buckle for the range of applied voltages, which would negatively impact tunability.

To characterize the tuning speed of the structures, we perform eigenfrequency studies within the cylindrically symmetric geometry. From the data tabulated in Table 1, we observe that the mechanical resonance shifts to higher frequencies with applied DC bias, an effect we attribute to the stress in the PZT causing a stiffening of the structure. For each design, the resonant frequency of the fundamental vibrational mode is between 500 to 1000 kHz. This represents an upper bound on the highest frequency component present in the driving electrical signal for quasi-static operation. Through direct digital synthesis and low pass RF filtering of the driving signal, we expect a switching time of 1 to  $10\ \mu\text{s}$  may be achieved.

#### 4. Experiment

Images of fabricated devices are shown in Fig. 4, and further fabrication details presented in the Appendix. Until now, we have considered only perfectly radially symmetric geometries. However, a practical ring resonator requires a bus waveguide to couple light into the ring. To achieve this, the release trench along the circumference of the resonator is interrupted, so that a bus waveguide may be run adjacent to the ring waveguide. The bus waveguide itself is also released to avoid leakage of the optical mode into the substrate. Due to intrinsic stress gradients within the oxide cladding and stress mismatch between oxide and the actuator, the released structure

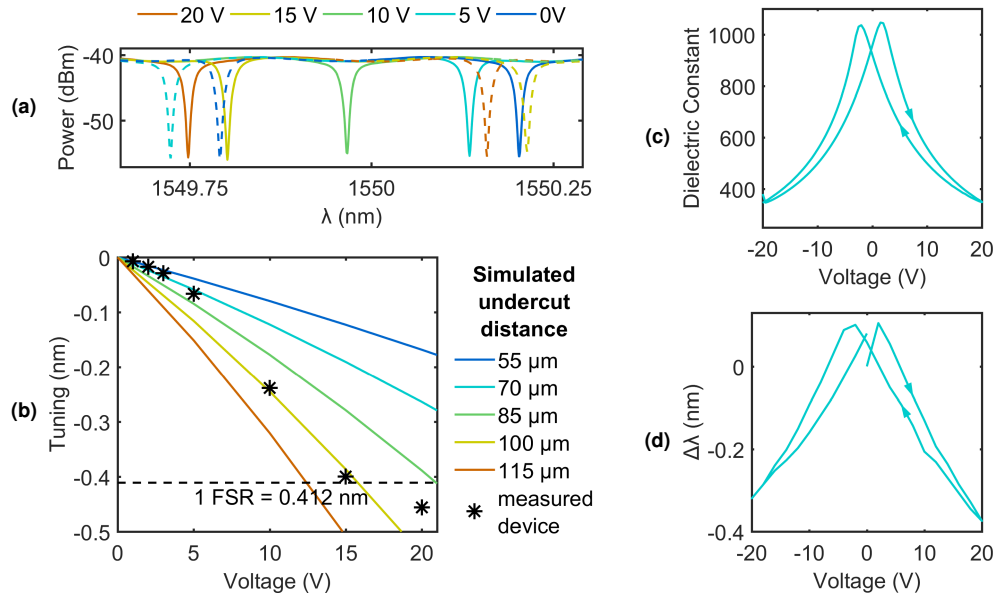


Fig. 5. Static tuning across a FSR is demonstrated.  $V_{FSR} = 16$  V. (a) Measured TM mode transmission spectra for the same device at various applied voltages. Adjacent notches are dashed to clarify the tuning of a single resonance in solid. (b) Simulated (lines) and measured (data points) tuning of TM mode versus voltage. Nonlinearity in tuning arises due to large mechanical deformation and hysteresis in the PZT. (c) PZT dielectric constant varies with the applied field and displays hysteresis, characteristic of ferroelectrics. Device area is  $0.01 \text{ cm}^2$ . (d) This hysteresis is observed in the ring resonator tuning as the electric field is reversed.

curls upwards and the waveguide core rotates, as demonstrated by simulation in Fig. 1(c), 1(d), and real device in Fig. 4(c). The height map in Fig. 4(d) reveals that the release distance is not uniform, due to irregular structure of the trenches through which  $\text{XeF}_2$  gas etches the silicon substrate isotropically for release. The undercut adjacent to the coupling regions, marked 2 in Fig. 4(d), is greater than  $155 \mu\text{m}$ , more than double the distance in regions spatially distant from coupling regions, marked as 1 in Fig. 4(d), of about  $75 \mu\text{m}$ .

The static tuning of the TM mode resonance as a function of applied voltage for the best device is shown in Fig. 5(a). For the measurement, a tunable laser source was coupled into on-chip waveguides through edge facets, and the response was measured by a photodetector at the through port. Electrodes were contacted by DC probes, and the spectrum was measured at each voltage bias. The device is tuned by a full FSR at 16 V applied bias, consistent with a simulated resonator of  $100 \mu\text{m}$  uniform undercut distance. In this device, however, the undercut, measured indirectly as in Fig. 4(d), was greater than  $200 \mu\text{m}$  adjacent the coupling region, and about  $86 \mu\text{m}$  away from the coupling region. This was the maximum amount of undercut achievable prior to structural failure due to the concentration of compressive stress at sharp features near coupling regions. In the simulated trace of Fig. 5(b), we observe that tuning is not perfectly linear. This is due to the rotational component of the deformation shown in Fig. 1(c), 1(d). The displacement of the cantilevered structure is normal to its surface, and thus as the displacement increases, a larger fraction of the incremental displacement lies in the radial direction. In the real structure however, the nonlinearity is more pronounced. This is due to the ferroelectric nature of PZT, which was not included in the simulation. The characteristic hysteresis of the dielectric constant, measured by the Sawyer-Tower method, is shown in Fig. 5(c), and the resultant hysteresis in the device

tuning is shown in Fig. 5(d).

The leakage current was below 10 nA, limited by equipment sensitivity, for voltages below 5 V. For biases above 5 to 10 V, we observe a gradually increasing leakage current versus time. Up to 20 V bias, devices remain operational for several minutes during which measurements were taken. At 25 V bias, instantaneous failure was observed. We credit this to abnormally high particulate count due to poor airflow from a PZT sol-gel deposition process optimized for 150 mm wafers rather than 100 mm wafers. This resulted in low dielectric strength and poor yield. For optimized processes, nA leakage currents at long-term sustained bias above 30 V are readily achieved [16–18].

Following the design of [12] for a high extinction ratio TM mode filter, we expect the high  $Q$  to be limited by coupling and coupler losses rather than propagation loss. We measure  $Q = 8.6 \times 10^4$  in the TM mode. Lower propagation loss and coupling in the TE mode yield  $Q = 1.0 \times 10^6$ . Ring resonator round-trip losses (including waveguide losses and coupling losses from add and drop ports) were estimated by fitting ring resonator spectral response to be 0.11 to 0.12 dB in the TE mode and 0.25 to 0.27 dB in TM mode, corresponding to an upper bound of 0.30 to 0.35 dB/cm for TE losses, and 0.65 to 0.75 dB/cm for TM losses. Absolute measures of waveguide loss are attainable through optical backscatter reflectometry (OBR) or cutback measurements, however no waveguide spirals of sufficient length for OBR could be measured due to low yield. For an identical released waveguide without any PZT processing, a waveguide loss of 0.12 dB/cm for the TE mode was measured by OBR, consistent with the results of [12]. We attribute the additional 0.1 to 0.2 dB/cm loss in the TE mode and 0.5 to 0.6 dB/cm loss in the TM mode both to coupling losses and extraordinary roughness and deep pitting of the SiO<sub>2</sub> upper cladding surface from C<sub>4</sub>F<sub>8</sub>/Cl<sub>2</sub> RIE etch used to pattern the PZT actuator. The TM mode is disproportionately impacted due to its lower core confinement and larger mode area, resulting in a larger interaction with the top cladding surface. For the same reason, the TM mode experiences a larger coupling coefficient, as well as larger coupling losses. AFM scan and SEM image of the top surface are shown in Fig. 4(e), 4(f). The peak-to-peak vertical deviation is greater than 200 nm, while the RMS roughness  $R_q$  is 20 nm. An alternative patterning processing using an Argon ion-mill etch to pattern the actuator followed by wet etch removal of an etch stop layer should reduce or eliminate top cladding surface roughness contribution to loss in future fabrication runs.

The small signal frequency domain response of the tuning was characterized by fixing the laser source wavelength to a value 3 dB below maximum transmission, near a resonance notch. A network analyzer supplies electrical input to tune the actuator, and analyzes the resulting electrical output response of the photodetector. The measurements were taken at 0 V DC bias. The device capacitance is 10 nF, the source output impedance is 50  $\Omega$ , and there is approximately 4  $\Omega$  parasitic resistance. This indicates an RC-limited response beyond 300 kHz. To obtain flat response to higher frequencies, a 10  $\Omega$  resistor is placed in parallel with the device to shunt the capacitance, increasing the RC frequency to about 1.3 MHz. The frequency response of the same device as in the heightmap of Fig. 4(d) is shown in Fig. 6(a). At mechanical resonance, we observe large enhancement of the tuning range. Furthermore, the frequency response exhibits many distinct features, which we ascribe to localized oscillations of the released waveguide membrane with frequency determined by the amount of undercut in the region of oscillation. For example, Fig. 6(e) shows the vertical displacement field for the lowest frequency resonance of a ring as measured by laser doppler vibrometry. The movement is localized to just the small region near the directional coupler where the undercut is largest. The relationship between undercut distance and mechanical resonance frequency is given in Fig. 6(b), where we model the vibrational eigenfrequencies as a function of undercut distance in a radially symmetric geometry. We ascribe the strong resonance peaks at 265 kHz, 359 kHz, and 430 kHz indicated by A in Fig. 6(a) to vibrations in areas adjacent to the coupling regions, where the undercut is 100 to 160  $\mu\text{m}$ . For this range of undercut distances, the model predicts fundamental vibrations (with shape as shown

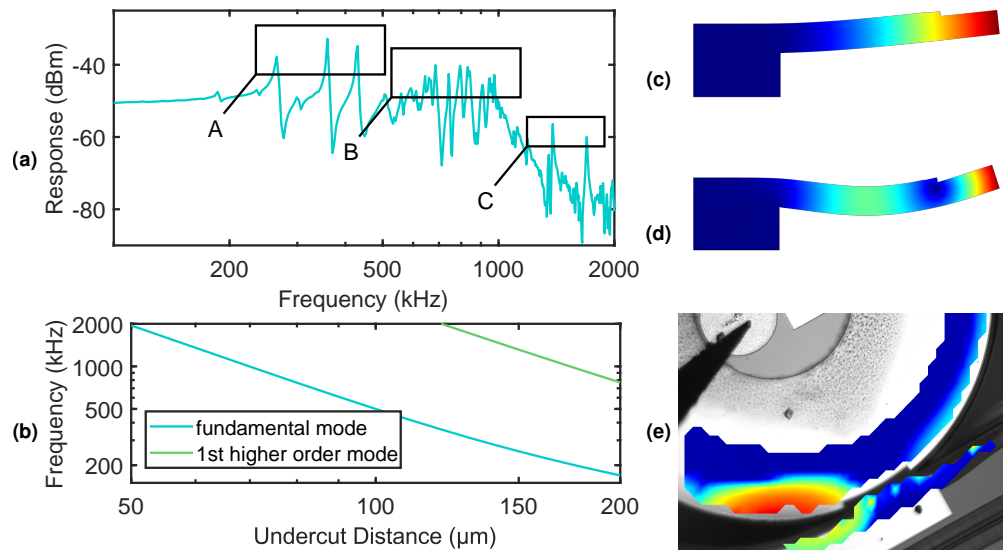


Fig. 6. (a) Measured resonator modulation response of the device in Fig. 4(d) with regions of interest indicated by A, B, and C. (b) Simulated vibrational eigenmode frequencies versus undercut. Fundamental (c) and first higher order (d) vibrational mode shapes, respectively. Redder colors indicate greater displacement from equilibrium. Simulated eigenfrequencies in (b) provide insight into the real resonances in (a). We ascribe A and C to fundamental and first order resonances of 100 to 160  $\mu\text{m}$  undercut areas, respectively. We ascribe B to fundamental vibrations of 80  $\mu\text{m}$  undercut areas. (e) Measurement by laser doppler vibrometry of the lowest frequency resonance. The movement is localized to the region of largest undercut.

in Fig. 6(c)) at 200 to 500 kHz. Distinct resonances at 1384 kHz and 1700 kHz correspond to higher order vibrations (in the shape of Fig. 6(d)) in the same physical regions. Many competing resonances indicated by B are present in the 600 to 1000 kHz range which we assign to regions away from the directional couplers where the undercut is consistently around 80  $\mu\text{m}$ . In the radial direction, these modes have the shape of the fundamental oscillation depicted in Fig. 6(c), but may have a significant wavevector component in the azimuthal direction with slight change in frequency, leading to the presence of many closely spaced resonances. The response falls off rapidly beyond 1 MHz, due to both RC limitations, and roll-off in the mechanical response.

## 5. Discussion

$V_\pi$  denotes the voltage required to induce a  $\pi$  phase shift (rather than  $2\pi$  for a full FSR). We observe that this condition is met for about 10 V in Fig. 6(a) in the TM mode. For the TE mode, whose tuning is within 4% of the TM mode, we also observe  $V_\pi = 10$  V. For a 580  $\mu\text{m}$  ring radius and TE waveguide loss of 0.3 dB/cm, we calculate  $V_\pi L = 3.6$  V cm, and  $V_\pi L\alpha = 1.1$  V dB. This value of  $V_\pi L$  is larger than values achievable with silicon or III-V phase modulators. However, taking into account optical losses through the  $V_\pi L\alpha$  figure of merit, these results demonstrate tuning efficiency at parity with current state-of-the-art phase modulators.

Free carrier plasma dispersion-based modulators in silicon can achieve modulation efficiency below 1 V cm for pn-junction or MOS capacitor devices [20–22]. However, free carrier absorption limits the propagation loss in these devices to above 10 dB/cm, and  $V_\pi L\alpha > 10$  V dB. Phase modulators based on III-V quantum wells may reach better efficiency, for example the III-V quantum well modulator demonstrated in [23] with  $V_\pi L = 0.09$  V cm, and loss of 20 dB/cm leads to a figure of merit  $V_\pi L\alpha = 1.8$  V dB. Recently, a III-V/Si MOS capacitor structure has achieved

$V_{\pi}L = 0.09$  V cm with 26 dB/cm loss [24].

Phase tuners using electro-optic polymers have also been demonstrated with extraordinarily low  $V_{\pi}L$  ( $< 0.1$  V cm), at the expense of high waveguide loss ( $> 10$  dB/cm) [25]. In [26], a  $V_{\pi}L$  of 0.62 V cm with loss of about 10 dB/cm was demonstrated. In [27], a  $V_{\pi}L = 0.052$  V cm was demonstrated, with waveguide loss of 40 dB/cm, for a  $V_{\pi}L\alpha$  of 2.08 V dB.

Ferroelectric ceramics with strong electro-optic (Pockels) effect have potential to reduce waveguide losses. By incorporating lithium niobate thin films on silicon,  $V_{\pi}L = 3.8$  V cm and  $\alpha = 1.2$  dB/cm have been achieved [28], yielding  $V_{\pi}L\alpha = 4.6$  V dB. In [29], a thin-film epitaxially grown BaTiO<sub>3</sub> modulator on MgO substrate was reported with  $V_{\pi}L = 1.25$  V cm, and less than 1 dB/cm loss, for  $V_{\pi}L\alpha = 1.25$  V dB. More recent work on epitaxially grown BaTiO<sub>3</sub> on silicon shows good modulation efficiency (1.5 V cm) but poor propagation loss (44 dB/cm) [30]. PLZT on sapphire [31] has demonstrated  $V_{\pi}L = 3$  V cm, and  $\alpha = 2.7$  dB/cm for a  $V_{\pi}L\alpha = 8.1$  V dB. Recent progress using PZT with lanthanide-based seed layer on a silicon substrate show impressive performance ( $V_{\pi}L = 1$  V cm,  $V_{\pi}L\alpha = 1$  V dB) however losses ( $\alpha \approx 1$  dB/cm) remain too high to qualify as ultra-low loss [32].

An interesting approach is the stress-induced Pockels effect in silicon waveguides [33], which could enable low-propagation-loss electro-optic phase tuning. The effect is extremely weak however; to date  $V_{\pi}L = 89$  V cm has been reported [34]. AlN is another interesting material platform for integrated photonics as it exhibits both piezoelectricity and Pockels electro-optic effect. In [35], low waveguide propagation loss of 0.6 dB/cm is reported, however the tuning efficiency is also low, tuning just 15 pm across 30 V applied bias. More recently [36], a tuning efficiency of  $V_{\pi}L = 240$  V cm has been reported.

Thermal phase shifters may be tuned by a full FSR down to extremely small device sizes and low voltage, however in this case, it is the power requirement that is prohibitive. In ultra-low-loss Si<sub>3</sub>N<sub>4</sub>, 200 to 500 mW are required per device [3]. In Si, 10 to 100 mW of power per device are typical, and 2.3 mW per FSR has been demonstrated with undercut waveguides at the expense of tuning speed (170  $\mu$ s) [2]. For applications requiring thousands of devices, even single mW of DC power per phase shifter becomes significant, and thermal crosstalk complicates system operation.

Prior to this work, optical MEMS based approaches have been explored by various authors. For example, in [37–39], ring resonators are tuned by electrostatic actuation of freestanding structures in the evanescent field of the waveguide. MEMS-actuated air-gap directional couplers have been explored to create more dramatically reconfigurable optical systems [40], including a  $50 \times 50$  crossbar switch [41]. Notably, in [42], a tunable ring cavity is formed by two fully suspended silicon waveguide sections linked by air-gap directional couplers. By lateral displacement of the waveguide sections relative to one another, an impressive tuning range of 10 nm is achieved. However, techniques such as those described above require complex structures within the mode of the waveguide that tend to increase scattering losses, and their applicability to low-loss waveguide platforms has yet to be demonstrated. In a similar vein, MEMS movable mirror approaches [43–46] have also been demonstrated, however these approaches require free propagation regions through air that add reflections and pose a challenge for integration into planar light-wave circuits.

Dynamic actuation of the stress field in a waveguide by PZT has also been explored [4,5,47–49], with the potential for lower optical losses than the air-gap-based MEMS approaches described above. Photoelastic modulation in a silicon-nitride-based low-loss platform has been demonstrated [5]. While the effect is weak ( $V_{\pi}L = 50$  V cm), the waveguide loss is low ( $\approx 0.1$  dB/cm), leading to a reasonable performance  $V_{\pi}L\alpha = 5$  V dB. Recently, in [50], an AlN piezoelectric actuator was deposited on a suspended silicon nitride waveguide to form a unimorph cantilever, in a geometry that bears similarity to this work. However, due to an unoptimized geometry and low piezoelectric constants of AlN relative to PZT, the tuning range is just 20 pm under 60 V bias. Though a radial displacement of 1 nm is claimed, the tuning exhibits large polarization dependence, indicating that tuning may be largely due to photoelastic index modulation, rather

than modulation of the physical length of the resonator. Thus, even among optical MEMS based approaches, phase tuning is largely performed by perturbing the waveguide effective index. Those works that explore perturbing the cavity size have done so by employing air-gaps, either in the form of free propagation regions [43–46] or suspended directional couplers [42]. To the best of the authors' knowledge, the in-plane component of macroscopic deformation in monolithic waveguides has been largely ignored until now.

Despite fabrication challenges which significantly degraded waveguide loss and limited the applied voltage, the figure of merit  $V_{\pi}L\alpha = 1.1$  V dB demonstrated in this work is already at parity with the best reported numbers across all technologies. However, in contrast to all approaches considered thus far (apart from thermal tuning), the tuning efficiency,  $V_{\pi}L$ , improves as the effective device size is reduced. Performance in the current demonstration was constrained by the intrinsic compressive stress of about  $-260$  to  $-320$  MPa in thermally grown and deposited  $\text{SiO}_2$  layers, leading to mechanical failure for large undercut. This is especially severe in the coupling regions, where asymmetry and sharp corners lead to high concentrations of stress. To bypass this limitation and take advantage of the favorable scaling of the effect with reduced size, we present the two optimized designs shown in Fig. 2(a), 2(b), discussed earlier. Notably, in the dual-stripe  $\text{Si}_3\text{N}_4$  based design, the combination of dual silicon nitride ( $> 800$  MPa tensile stress) layers within an oxide cladding of comparable thickness serve to balance the overall stress in the structure. For the silicon-on-insulator based design, the silicon itself is stress-free.

With regards to excess waveguide loss caused by the PZT fabrication and release processes, we note that no excess loss was observed in structures without PZT processing, as mentioned earlier. Furthermore, released structures have been demonstrated with quality factors up to 875 million for freestanding resonators, and 200 million with integrated bus waveguides [51, 52]. While  $\text{XeF}_2$  gas used for release is known to slowly attack  $\text{SiO}_2$  in the presence of Si [53], there is no evidence of roughening of the  $\text{SiO}_2$  surface. Thus, if the top-surface  $\text{SiO}_2$  can be protected from PZT processing by the method proposed earlier, this phase tuning technique may be applied with zero excess waveguide loss.

The propagation loss for dual stripe  $\text{Si}_3\text{N}_4$  waveguides was reported in [11] to be 0.08 to 0.09 dB/cm. In the modified design presented here, the core confinement is within a 10% of the core confinement of the original design. Thus, we expect that scattering loss at the core-cladding interface should be roughly identical in both configurations. For a hypothetical dual stripe design with 0.09 dB/cm loss, 80  $\mu\text{m}$  bend radius, and tunable by a FSR with 30 V applied bias, or a half-wave voltage of about 20 V, we estimate  $V_{\pi}L = 1$  V cm and  $V_{\pi}L\alpha = 0.09$  V dB. For the silicon-based design with ring radius 45  $\mu\text{m}$ , we estimate a  $V_{\pi}L = 0.57$  V cm. A conservative estimate of 1 dB/cm for deeply etched Si waveguides would yield  $V_{\pi}L\alpha = 0.57$  V dB, however, shallow etched silicon waveguides with sub 1 dB/cm loss have been demonstrated [54–56], which could potentially push performance into  $V_{\pi}L\alpha < 0.1$  V dB range. Similarly, recently improvements in high-confinement silicon nitride waveguides [57] have yielded  $\alpha < 0.01$  dB/cm waveguide loss at similar bend radii. Applying this approach to such low-loss waveguides would allow a further order-of-magnitude improvement in  $V_{\pi}L\alpha$ .

## 6. Conclusion

We have presented a novel phase tuning approach by geometric deformation with ultra-low power operation and tunability that scales favorably with reduced device size. In a proof-of-concept demonstration, we have already demonstrated performance at parity with state-of-the-art published results, with a clear path towards a further improvement by an order of magnitude. We expect this work to primarily be of interest to the ultra-low-loss community, and especially for the RF photonics community where low propagation loss is critical, and bend radii of 100  $\mu\text{m}$  and above are typical. If our proposed design down to 45  $\mu\text{m}$  bend radius may be experimentally realized, this would enable thousands of devices to be integrated on a single 20 mm by 20 mm

die, with applications such as wavelength-selective crossbar switches, and optical phased arrays for LIDAR.

### Appendix: Fabrication

The fabrication of waveguides begins by forming a 4  $\mu\text{m}$  thick lower cladding by thermal oxidation of a 100 mm diameter prime Si wafer. 175 nm of stoichiometric  $\text{Si}_3\text{N}_4$  is deposited by low-pressure chemical vapor deposition. The 2.2  $\mu\text{m}$  wide waveguide core is defined by deep ultra-violet lithography and etched by inductively-coupled-plasma (ICP) reactive ion etch (RIE) with  $\text{CHF}_3/\text{O}_2/\text{CF}_4$  gases. An upper cladding of  $\text{SiO}_2$  is formed by plasma-enhanced chemical vapor deposition (PECVD), and annealed at 1050  $^\circ\text{C}$  for seven hours.

The fabrication of the actuator [58] begins by planarizing the top cladding by chemical-mechanical polishing to 1.5  $\mu\text{m}$  thickness. This step is critical to ensuring crack-free deposition of the PZT. To form the actuator, Ti is sputtered and oxidized to form a 35 nm seed layer of  $\text{TiO}_2$  [59]. This forms a template to sputter a 100 nm Pt lower electrode. A PZT film with a Zr/Ti ratio of 52/48 is then deposited by chemical solution deposition (CSD) [58, 60, 61] and heated to 700  $^\circ\text{C}$  for 2 minutes by rapid thermal annealing in flowing oxygen to crystallize the film. The process is repeated several times to form a 1  $\mu\text{m}$  thick, (001) oriented polycrystalline film, with grain size on the order 100 nm. The actuator is capped by a 100 nm Pt top electrode and patterned in three RIE steps by  $\text{C}_4\text{F}_8/\text{Cl}_2$  gases. The first step etches the top electrode. The second step etches through the PZT and lower electrode to stop on  $\text{SiO}_2$ . The third step etches through the PZT to access the lower electrode. Next, a contact metallization comprised of 730 nm Au/20 nm Pt/20 nm Ti is deposited by electron beam evaporation and patterned by lift-off.

Finally, deep trenches are etched adjacent to the waveguides through the  $\text{SiO}_2$  to access the Si substrate for release using ICP RIE with  $\text{CHF}_3$  etch gas. The wafers are diced and the facets polished and coated by ion-beam deposition with a 250 nm layer of  $\text{SiO}_2$ . In the final step prior to testing and measurement,  $\text{XeF}_2$  gas etches the exposed Si substrate through the deep trenches in order to undercut and release the waveguides.

### Funding

Morton Photonics Air Force SBIR program (contract #FA8650-15-C-1863); Keysight Laboratories.

### Acknowledgements

We thank Michael Davenport, Tin Komljenovic, Alexander Spott, Eric Stanton, Nicolas Volet, and Taran Huffman for helpful discussions. We are grateful to Carl Meinhart for his finite element simulation expertise, and to Kimberly Turner and Nicholas Bousse for use of their Laser Doppler Vibrometer. We thank Dr. Ryan Rudy, Joel Martin, and Brian Power of the US Army Research Laboratory and Steven Isaacson from General Technical Services for their contributions to the device fabrication and electrical characterization.